CrystEngComm

ROYAL SOCIETY OF CHEMISTRY

PAPER

View Article Online
View Journal | View Issue

Cite this: *CrystEngComm*, 2024, **26**, 32

Perpendicular magnetic anisotropy and magneto-optical properties of Bi,Mn:YIG epitaxial films†

Jiewen Jiang,[ab] Yun Dai,[ab] Jiamin Shang,[ab] Zhen Zhang,[ab] Liangbi Su,[ab] Maojie Cheng,[c] Dunlu Sun,*[c] A. Stupakiewicz[d] and Anhua Wu*[ab]

Films with perpendicular magnetic anisotropy have obvious storage performance advantages, so being able to easily change the direction of magnetization of a $Y_3Fe_5O_{12}$ (YIG) film is an important aim in the field of photo-magnetic storage. A series of Bi,Mn co-doped $Y_3Fe_5O_{12}$ films with good crystallinity and great magneto-optical properties, were prepared *via* the liquid phase epitaxial method. These films are pseudomorphic structures in the substrate and have high perpendicular magnetic anisotropy. By comparing the change in the calculated magnetic anisotropy and the actual magnetic anisotropy, with Mn^{3+} content, we see that: the stress-induced magnetic anisotropy increases with the increase of lattice mismatch; on the other hand, with increasing Mn^{3+} content, the magnetostriction effect decreases first and then increases, which reflects the regulation effect of Mn^{3+} and lattice mismatch on the perpendicular magnetic anisotropy. Finally, the magnetic anisotropy field (>3000 Oe) is higher than that of Mn:YIG (<1000 Oe) as previously reported.

Received 29th July 2023,
Accepted 7th November 2023

DOI: 10.1039/d3ce00760j

rsc.li/crystengcomm

1 Introduction

Recently, ferrimagnetic garnet crystals shown potential in studies of magnetization dynamics induced by external stimuli from laser and electrical current/field pulses. Due to their room temperature magnetic ordering, high transmittance in the near-infrared band and good magneto-optical properties, $Y_3Fe_5O_{12}$ (YIG) films have aroused extensive research interest for optical and magneto-optical device applications. In spin polarizer,[1] spin-torque oscillator,[2] magnonics devices,[3] non-volatile photo-magnetic[4] and optical-magnetic storage,[5] a perpendicular magnetic anisotropic YIG film with an easily accessible out-of-plane (OP) magnetization axis is advantageous. Therefore, changing the direction of the magnetization axis of YIG films is one of the most important research directions to realize YIG functional materials in storage research.[6–10] The magnetic anisotropy of the film is mainly composed of magnetocrystalline anisotropy, shape anisotropy, stress-induced anisotropy, *etc.* Utilizing the lattice distortion and magnetoelastic effect, the film can acquire perpendicular magnetic anisotropy (PMA),[11–13] while Mn^{3+} ion has a strong magnetoelastic effect.[14] At present, the research into Mn:YIG (MYG) has mostly concentrated on microwave fields and ceramic fields in which the Mn^{3+} ion is used to improve magnetic properties and reduce loss. There is only a small amount of research on changing anisotropy. For example, by growing YIG films on $Y_3Al_5O_{12}$ (ref. 13) or quartz[15] substrates with different thicknesses, it is found that the OP magnetocrystalline anisotropy reflects the tetragonal symmetry of the garnet lattice, which requires a large lattice strain. It has been suggested that doping with strong spin–orbit coupling ions such as Dy^{3+}, Bi^{3+}, Tm^{3+} induces controllable magnetic anisotropy,[16] and Bi^{3+},Dy^{3+} co-doped YIG [17] and $Tm_3Fe_5O_{12}$ (ref. 18) have been reported that possess PMA properties; Jahn–Teller ions such as Mn^{3+} have also been used as dopants, and improve the magnetoelasticity of YIG [14,19] (magnetostriction coefficient of pure YIG is -2.22×10^{-6} (ref. 20)). Although the PMA can be regulated by Mn^{3+},[21] the concentration of Mn^{3+} required is large (x = 1.12) and the obtained magnetic anisotropy field is small. Therefore, combined with the above two methods to improve the PMA, Bi^{3+} can reduce the concentration of Mn^{3+} required for PMA. At the same time, it can raise magneto-optical properties, which is favorable for utilizing the Kerr effect to read storage information. Using such methods, YIG films with PMA can play a role in many fields, such as spintronic devices,

[a] *State Key Laboratory of High Performance Ceramics and Superfine Microstructure, Shanghai Institute of Ceramics, Chinese Academy of Sciences, Shanghai 201899, China. E-mail: wuanhua@mail.sic.ac.cn*
[b] *Center of Materials Science and Optoelectronics Engineering, University of Chinese Academy of Sciences, China*
[c] *Crystal Lab of Laser Technology Research Center, Anhui Institute of Optics and Fine Mechanics, Hefei Institutes of Physical Science, Chinese Academy of Sciences, Hefei, 230031, P. R. China. E-mail: dlsun@aiofm.ac.cn*
[d] *Faculty of Physics, University of Bialystok, Ciolkowskiego 1L, 15-245 Bialystok, Poland*

† Electronic supplementary information (ESI) available. See DOI: https://doi.org/10.1039/d3ce00760j

photo-magnetic storage, magneto-optical or microwave devices, and so on.[22,23]

Growth methods of YIG single crystal films include pulsed laser deposition (PLD), radio frequency magnetron sputtering (RFMS), chemical vapor deposition (CVD) and liquid phase epitaxy (LPE). Using LPE method,[24] the melt creates a supersaturation state, which preferentially nucleates and grows on the single crystal substrate to directionally form the single crystal. According to the contact between the melt and the substrate, the LPE method can be divided into the tipping method,[25] the rotating method[26] and the dipping method,[27] and the last includes the horizontal dipping method and the vertical dipping method. Compared with other methods, the LPE method has the advantages of high growth rate, easy and diverse ion doping, high crystalline quality, and the ability to prepare a thick film, which is the main choice for large area preparation and industrial production of YIG. However, the LPE method also has some problems such as: poor uniformity, rough surface, and lattice mismatch, *etc.*

The key questions are how Mn^{3+} ions and the lattice mismatch brought by Bi^{3+}, affect the perpendicular magnetic anisotropy and how to maximize the perpendicular magnetic anisotropy of the YIG films. Therefore, we studied the change in perpendicular magnetic anisotropy with different Mn^{3+} content, and finally obtained film samples with good magneto-optical properties and a larger perpendicular magnetic anisotropy than reported in ref. 21.

2 Experimental

Y_2O_3, Fe_2O_3, Bi_2O_3, Mn_2O_3 powders with 4 N purity were selected as the raw materials, B_2O_3 and PbO were used as fluxes, in which Bi_2O_3 is both a flux and a dopant. After weighing the raw materials, they were milled, put into a crucible and sintered at 1350 °C for 12 h. The (111) oriented $(GdCa)_3(GaMgZr)_5O_{12}$ (SGGG) substrate was used and is more suitable for epitaxial growth of high Bi doped YIG (BYG) than that of gadolinium gallium garnet (GGG) substrate. In this experiment, the horizontal dipping method was mainly used. We put the synthetic polycrystalline raw materials into a platinum crucible and placed in a furnace. The platinum triangle fixture was moved to the center of the crucible, so that the substrate located in the center of the melt to ensure uniform growth. The raw materials were melted and insulated for 2 h, above the saturation temperature (1200 °C), so that they fully melted and mixed. When they were cooled, the step-cooling method rather than the ultra-cooling method was adopted, resulting in higher crystalline quality, and they were dropped to below the saturation temperature to supersaturate the high temperature melt. The substrate needs to be pre-pickled and cleaned with the absolute ethyl alcohol in order to slightly erode the surface of the substrate, open the molecular bond and activate the surface, and then we placed it above the melt to preheat. The YIG films were obtained at a growth temperature (T_g) of about 1125–1175 °C, growth rotation rate (ω_g) of 35–75 rpm and growth time (t_g) of 2 h. After the growth, high-speed revolutions (ω) were used to remove the residual melt, and the films were treated with hydrochloric acid to further remove the residual melt. Maintaining a small angle tilt when the substrate rotates, was beneficial to remove the residual melt, and maintaining the periodic positive and negative rotation was also conducive to the uniform growth of the films. Because YIG would undergo a peritectic reaction at high temperature and is an incongruent melting compound, flux was needed to reduce the melting point in order to easily grow the single crystal. The PbO was generally used in the growth of the YIG, but in the growth of BYG, the Bi_2O_3 can play the role of the flux, however its viscosity is large. The combination of the two fluxes is better and can results in more Bi^{3+} ion doping. In addition, due to the consumption of raw material and the volatilization of PbO when growing, periodic supplements were needed to ensure the element composition consistency of the epitaxial films.

The crystal structure of the films was measured using an X-ray diffractometer. The microstructure observation was performed using scanning electron microscopy. We used a physical property measurement system (SQUID) to measure the magnetization. The magneto-optical properties were studied using the Malus law.

3 Results and discussion

3.1. Growth process and process parameters

A series of $(Y_{3-x}Bi_x)(Fe_{5-y}Mn_y)O_{12}$ film samples were successfully prepared using the LPE process. Table 1 shows the process parameters of epitaxial growth and composition of samples. Through trying to grow samples BYG01, BYG02a, BYG02b, BYG03, we finally found an optimal process route for preparing YIG films. By growing at 1125 °C for 1 h, stirring at 60 rpm, removing the residual melt at 120 rpm after raising the substrate, and then undergoing corrosion and polishing, we obtain samples BYG03, BMYG04, BMYG05, BMYG06 and BMYG09 with good crystalline quality (ESI† Fig. S1). Samples (BYG03, BMYG04, BMYG06, BMYG09) have different Mn^{3+} content (y = 0, 0.08, 0.16, 0.28, respectively) to regulate their magnetic properties. Because Bi_2O_3 also acts as a flux, it is difficult to precisely control the Bi^{3+} content.

Holmquist[28] has studied the YIG phase first formed at 600 °C, and the single-phase YIG was formed completely at 1200 °C (melting temperature (T_m) was 1200 °C), while Nazlan and Fang[29,30] found that YIG could be fully crystallized at 1100 °C. Ali[31] has studied the formation process of YIG at high temperatures, as shown in Fig. 1. From the outside to the inside, yttrium iron perovskite ($YFeO_3$, YIP) is formed first on the surface, and then YIG is generated. Only when the temperature is higher than 1150 °C, does Fe^{3+} have enough energy to diffuse into the Y_2O_3 phase to continue the reaction. When YIP is converted to YIG, it needs to react with Fe_2O_3, so the iron-rich melt is easier and quicker to generate YIG. This is also confirmed in Fig. 2, which compares the

Table 1 Growth process parameters and composition of $(Y_{3-x}Bi_x)(Fe_{5-y}Mn_y)O_{12}$ samples created using horizontal dipping unless otherwise stated. Detailed results of the compositional analysis are provided in the ESI† (Table S1)

Samples	T_g/°C	t_g/min	ω_g/rpm	ω/rpm	Thickness/μm	$x_{Bi}(x_{Bi}\%)$	y_{Mn}
BYG01	1000	120	100	400	—	—	—
BYG02a	1150	10	75	120	—	—	—
BYG02b[a]	1175	10	15	30	—	—	—
BYG03	1125	60	60	120	60.2	0.34(11.33)	0
BMYG04	1125	60	60	120	35.2	0.19(6.33)	0.08
BMYG05[a]	1125	90	45	75	19.1	0.25(8.33)	0.07
BMYG06[a]	1125	60	45	75	20.1	0.11	0.16
BMYG09	1125	60	60	120	55.0	0.10	0.28

[a] Vertical dipping.

XRD patterns of the raw material after solid-phase reaction, with the standard result of YIG (JCPDS: 43-0507) and YIP (JCPDS: 39-1489) and marks the peaks corresponding to the plane. We performed reactions multiple times at 1350 °C for 1 h, to completely convert the raw materials to the pure YIG phase.

We compared the growth rates of the vertical dipping and the horizontal dipping and their effects on defects. With the increase of growth rate, the Bi^{3+} content increased, the lattice tensile stress decreased, and the morphology of defects changed from cracks to pits.[32–34] The pits slightly increase the optical absorption, but have little impact on the magnetic properties, horizontal dipping can be used to improve the crystalline quality of the YIG films.

3.2. Lattice mismatch and perpendicular magnetic anisotropy

Fig. 3 shows the XRD patterns of the films. It shows that the samples have only one peak (444) (Fig. 3(a)), indicating that the epitaxial growth is good, and the growth direction of samples is along the direction of the substrate (by calculation, the left peak is $K_{\alpha1}$, and the right peak is $K_{\alpha2}$). Through locally enlarged patterns of 50–52°, it can be found that with the increase of Bi^{3+} content, the diffraction peaks shift to the left and the lattice constant increase, see Fig. 3(b). This indicates that large-size ions (Bi^{3+}) basically enter the lattice to replace Y^{3+}. The lattice mismatch between the epitaxial film and the substrate is less than 1% (generally, the lattice mismatch of heteroepitaxy is less than 5–10%,[35] and high-quality YIG films require GGG substrates with similar structures and a very small lattice mismatch (<0.06%)[36]).

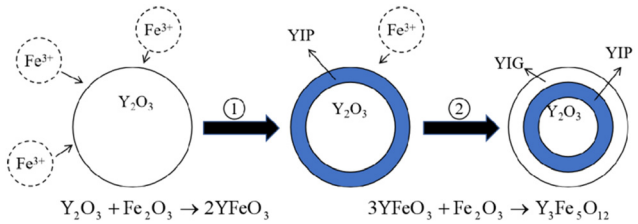

Fig. 1 Schematic diagram of the formation process of YIG.

The reciprocal space mapping shows that the films have a pseudomorphic structure (see Fig. 4). The in-plane lattice constant of the films is equal to that of the substrate. On the one hand, the formation of this pseudomorphic structure is caused by the lattice mismatch between the films and the substrate, on the other hand the magnetostriction effect also plays a role.

For epitaxial films, the YIG is paramagnetic above the Curie temperature. When the temperature is lower than the Curie temperature, spontaneous magnetization is generated due to the exchange interaction, thus generating spontaneous magnetostriction. Since the magnetostriction coefficient of pure YIG is negative, the lattice will be compressed along the direction of magnetization. Since all the prepared samples have PMA except BMYG04 (see Fig. 6), the direction of magnetization is in the perpendicular direction, which facilitates the horizontal stretching and the formation of pseudomorphic structures, see Fig. 5. For sample BMYG04, the effect is the opposite, so we have a negative value when calculating the contribution of its magnetostriction to the magnetic anisotropy. We first consider the surface effect on the magnetic anisotropy of the sample. According to the

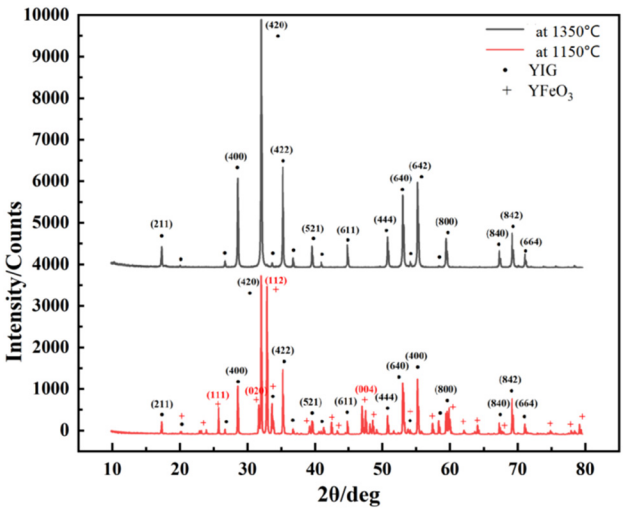

Fig. 2 XRD patterns of raw material after solid-phase reaction at high temperature (1350 °C) and low temperature (1150 °C).

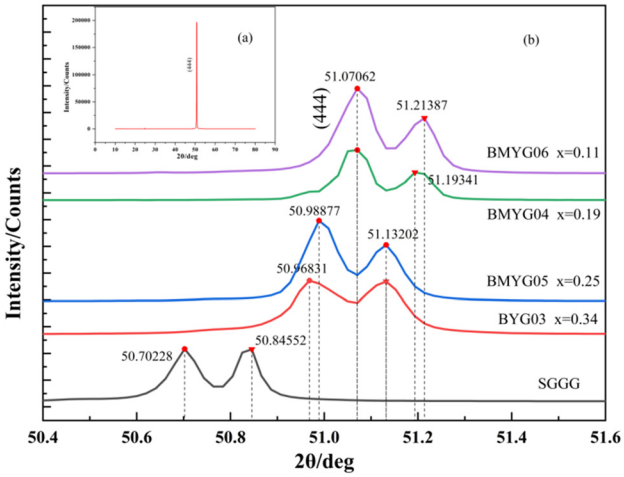

Fig. 3 (a) XRD patterns of the samples (BYG03, BMYG04, BMYG05, BMYG06), (b) locally enlarged XRD patterns of the samples from 50° to 52°.

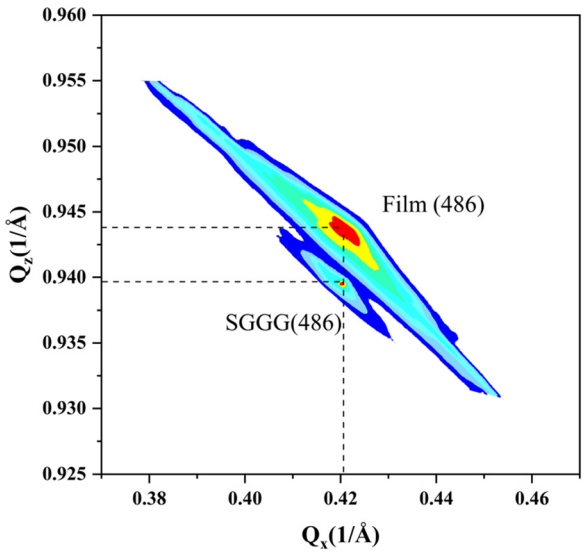

Fig. 4 The reciprocal space mapping of the samples.

formula[37,38] $E_{total} = (\gamma_s + \gamma_i)/h + M_{hkl}\varepsilon^2$ (where h is the thickness of the sample), the surface effect is inversely proportional to the thickness of the sample, which means that the surface effect in YIG is only about one thousandth that of the literature values and is negligible.

According to the theory of pseudomorphic structures,[39] we can calculate parameters such as lattice mismatch and lattice strain. The calculation procedure is shown in the ESI† (eqn (S1)–(S7)), and the results are shown in Table 2. The calculated in-plane lattice constants of the films are basically consistent with those of the substrate, which verifies the correctness of the theory and parameter values. Since the in-plane lattice strain of the YIG films is within 0–0.5%,[40] stress-induced perpendicular magnetic anisotropy is more easily generated. Later we use these data to further calculate the value of the stress-induced magnetic anisotropy.

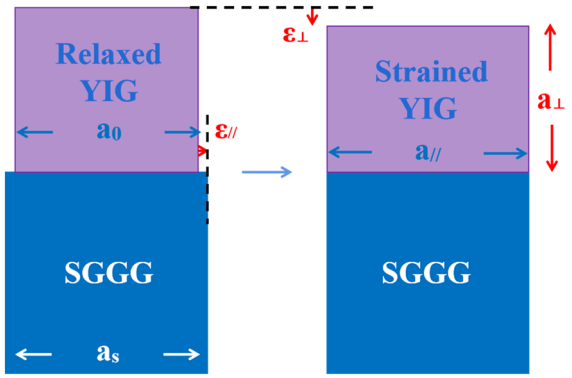

Fig. 5 Schematic diagram of the lattice mismatch and lattice strain in the pseudomorphic structure.

Fig. 6 shows the hysteresis loops of the YIG epitaxial films. It can be seen from Fig. 6(a) that all samples exhibit strong saturation magnetization and low coercivity, indicating the soft magnetic properties of the YIG materials. The saturation magnetization increases first and then decreases with increasing Mn^{3+} content, indicating that Mn^{3+} ions preferentially occupy the octahedral sites, because the magnetic moment of Mn^{3+} is smaller than that of Fe^{3+}. We measured the hysteresis loops of the samples in the IP and OP directions at room temperature, as shown in Fig. 6(b–e). Except for BMYG04, the samples show a large PMA. With the increase of Mn^{3+} content, the magnetic anisotropy field of the samples changes. On the one hand, the Bi^{3+} content decreases and the lattice strain increases. And the positive in-plane lattice tensile strain ($0 < \varepsilon_{//} < 0.5\%$)[39] makes the OP magnetic anisotropy stronger. On the other hand, the Mn^{3+} ion makes the magnetoelastic coefficient of the samples change from negative to positive and its absolute value becomes smaller, which makes the OP magnetic anisotropy lower. So both lead to the phenomenon of BMYG04 not having PMA. In contrast to the contribution of large-size ions (Bi^{3+}) to PMA, the magnetoelastic ions (Mn^{3+}) do not directly change the lattice constant and do not reduce the crystallinity.

From the above theoretical model, we calculate the magnetic anisotropy caused by the lattice mismatch and magnetostriction and compare it with the actual magnetic anisotropy. The calculation procedure of the magnetic anisotropy is shown in the ESI† (eqn (S8)–(S10), Table S2, Fig. S2). The actual magnetic anisotropy and calculated magnetic anisotropy first decrease and then increase with the increase of Mn^{3+} content, reflecting the regulatory effect of Mn^{3+} and lattice mismatch on PMA. On the one hand, with the increase of lattice mismatch, the stress-induced magnetic anisotropy increases; on the other hand, with the increase of Mn^{3+} content, the magnetoelastic constant changes from negative to positive, and the magnetostriction effect decreases first and then increases. From the comparison of the magnetic anisotropy constant and the magnetic anisotropy field (see Fig. S1†), we can see that the decrease of the magnetic

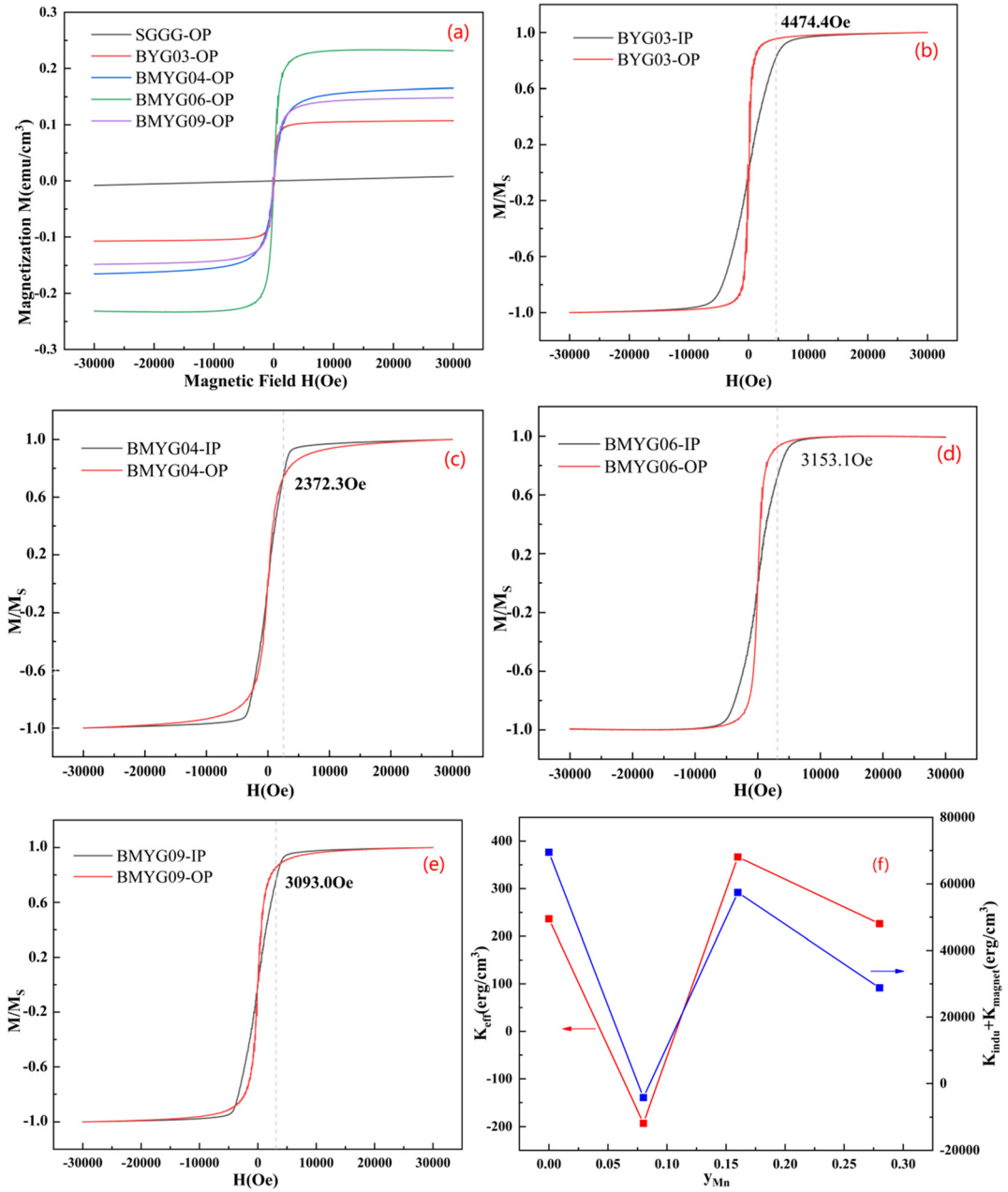

Fig. 6 (a) Hysteresis loops of the epitaxial films, (b–e) hysteresis loops of the epitaxial films in the IP and OP directions, (f) actual magnetic anisotropy (red line) and the calculated magnetic anisotropy (blue line) against the Mn^{3+} content. The contribution of paramagnetic substrate has been removed from the hysteresis loops of the films.

Table 2 The calculated values of lattice constant, lattice strain, lattice stress and lattice mismatch of $(Y_{3-x}Bi_x)(Fe_{5-y}Mn_y)O_{12}$ samples ($a_{f\perp}$: out-of-plane lattice constant of the strained film; a_S = 12.463 Å: lattice constant of the substrate; a_{f0}: lattice constant of the relaxed film; $\varepsilon_{//}$: in-plane lattice strain; $\sigma_{//}$: in-plane lattice stress)

Samples	2θ/deg	$a_{f\perp}$/Å	a_{f0}/Å	$10^4\varepsilon_{//}$	$\sigma_{//}$/GPa	Lattice mismatch/%	$a_{f//}$/Å
BYG03	50.96831	12.400	12.428	+26.674	+0.754	−0.281	12.461
BMYG05	50.98877	12.398	12.427	+27.628	+0.781	−0.289	12.461
BMYG04	51.07062	12.3815	12.418	+34.799	+0.983	−0.361	12.461
BMYG06	51.07062	12.379	12.416	+35.281	+0.997	−0.377	12.460
BMYG09	51.05016	12.3865	12.4205	+0.32409	+0.916	−0.341	12.461

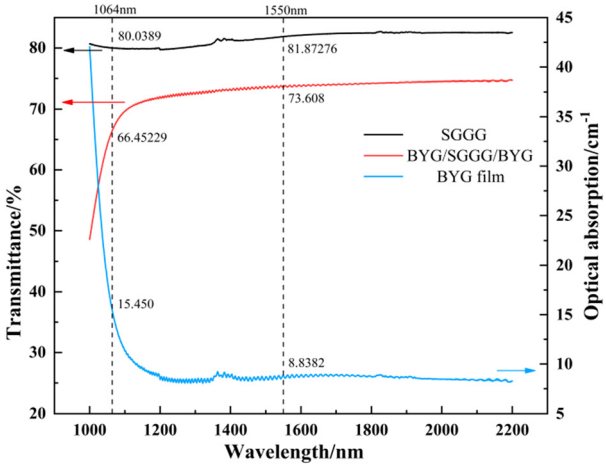

Fig. 7 The transmittance spectrum and the calculated absorption spectrum of the epitaxial film at the wavelength 1000–2200 nm. The fluctuation at 1400 nm in the calculated absorption spectrum is caused by replacing the light source when measuring the substrate, there is no peak above 1200 nm in the transmittance spectrum.

anisotropy of sample BMYG09 is mainly caused by the decrease of its saturation magnetization. Because its magnetic anisotropy field is basically unchanged. Finally, the magnetic anisotropy field (>3000 Oe) is higher than that of Mn:YIG (<1000 Oe) as reported in the ref. 21.

3.3. Transmittance spectrum and magneto-optical hysteresis loops

Fig. 7 shows the transmittance spectrum of the epitaxial films at wavelength 1000–2200 nm. The transmittance of the samples is 73.608% at 1550 nm, and the optical absorption coefficient at 1550 nm calculated without considering the reflection is 8.838 cm^{-1}. The film has no obvious absorption peak at wavelength 1200–2200 nm and has a low absorption coefficient,[41] which is favorable for magneto-optical applications.

Fig. 8 shows the Faraday effect of the samples BYG03, BMYG04 and BMYG05. It can be described by the Verdet constant and the specific Faraday rotation angle as

$$\theta = VHL \quad (1)$$

$$\theta_F = \theta/L \quad (2)$$

where θ is the Faraday rotation angle, H is the intensity of the applied magnetic field, and L is the thickness of the samples. As can be seen in Fig. 8(b), the samples mainly show soft magnetic properties with low coercivity, which is consistent with the hysteresis loops (see Fig. 6). Fig. 8(c) shows the Verdet constants of the BYG03 (x = 0.34, x_{Bi} = 11.33%), BMYG04 (x = 0.19, x_{Bi} = 6.33%) and BMYG05 (x = 0.25, x_{Bi} = 8.33%) samples, at the different wavelengths. The

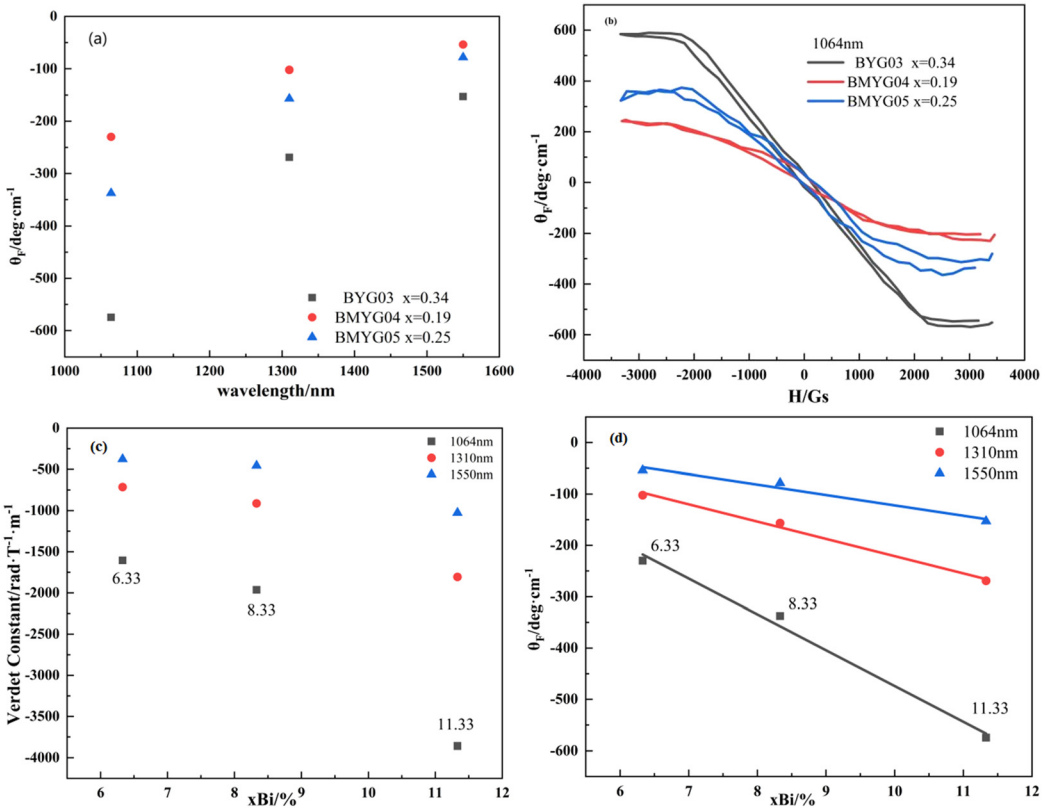

Fig. 8 (a–d) Magneto-optical loops of the samples and the Verdet constant and Faraday rotation angles of BYG and BMYG against ion content. The H direction is oriented perpendicular to the surface of the sample.

Verdet constant of the sample is calculated at the saturation field (about 0.25 T). The Faraday rotation angle of pure YIG is positive, and the Verdet constant becomes larger and negative with the increase of Bi^{3+} content. Its Verdet constant is 10^3 orders of magnitude, much higher than commercial materials such as TGG. Since the Bi^{3+} content of the BMY06 is only 4%, its Faraday rotation angle is around the 0 value, and so its Faraday rotation angle was not detected. Fig. 8(d) shows that the specific Faraday rotation angle changes linearly with the increase of Bi^{3+} content. While the Bi^{3+} content increases to ~1.0 at%, the θ_F value increases to about −69.7 deg cm^{-1}, −33.7 deg cm^{-1} and −20.2 deg cm^{-1} at 1064 nm, 1310 nm and 1550 nm, respectively. The specific mechanism of the higher Faraday rotation angle can be interpreted as: 6p energy level of Bi^{3+} (1.6 eV) is very close to the 3d energy level of Fe^{3+} (1.52 eV) and the 2p energy level of O^{2-}. Orbital hybridization increases the split of the excited state and the oscillator strength of the charge transfer transition.[42] Therefore, the magneto-optical effect will be enhanced, which will facilitate the application of YIG materials in the magneto-optical field.[43,44]

4 Conclusions

In summary, a series of Bi and Mn co-doped $Y_3Fe_5O_{12}$ epitaxial films with good magneto-optical properties and good perpendicular magnetic anisotropy, were successfully prepared using the liquid phase epitaxy method. The results obtained are as follows:

1. To improve the crystalline quality, Bi,Mn co-doped YIG films were obtained using methods such as reacting multiple times at 1350 °C for 1 h to completely convert the raw materials to a pure YIG phase, horizontal dipping.

2. The prepared films have greater perpendicular magnetic anisotropy than those found in the literature. By comparing the changes of the calculated value and the actual value with Mn^{3+} content: on the one hand, the stress-induced magnetic anisotropy increases with the increase of lattice mismatch; on the other hand, with the increase of Mn^{3+} content, the magnetostriction effect decreases first and then increases, which reflects the regulation effect of Mn^{3+} and lattice mismatch on the perpendicular magnetic anisotropy. So we believe that the perpendicular magnetic anisotropy will be stronger with the increase of the Mn^{3+} content, which will facilitate the application of YIG materials in spintronic devices or magneto-optical storage.

3. Bi^{3+} can improve the magneto-optical properties of the YIG materials. The specific Faraday rotation angle and the Verdet constant of Bi,Mn:YIG are −574.75 deg cm^{-1} and −3858.18 rad/$(T \times m)$ at 1064 nm, and the specific Faraday rotation angle is proportional to the Bi^{3+} content.

Author contributions

J. J., A. W., L. S., and D. S. conceived the project, wrote the paper, and were primarily responsible for the experiment. J. J., Y. D., and M. C. were responsible for the growth of YIG films. J. J., Z. Z., and J. S. carried out the experiments on transmittance and magneto-optical performance. J. J., and A. S. were responsible for the discussion of the effects of ion doping on magneto-optical properties and perpendicular magnetic anisotropy. All authors have given approval to the final version of the manuscript.

Conflicts of interest

There is no conflict of interest in this manuscript.

Acknowledgements

This work was supported by the National Key R&D Program of China (2021YFB3602503), the National Natural Science Foundation of China (52272014), Science and Technology Commission of Shanghai Municipality (21520711300, 20520750200). This work was also supported by the CAS Project for Young Scientists in Basic Research (YSBR-024) and the International Partnership Program of Chinese Academy of Sciences (121631KYSB20200039).

References

1 A. D. Kent, B. Ozyilmaz and E. del Barco, *Appl. Phys. Lett.*, 2004, **84**, 3897–3899.
2 D. Houssameddine, U. Ebels, B. Delaet, B. Rodmacq, I. Firastrau, F. Ponthenier, M. Brunet, C. Thirion, J. P. Michel and L. Prejbeanu-Buda, *et al.*, *Nat. Mater.*, 2007, **6**, 447–453.
3 V. Kruglyak, S. Demokritov and D. Grundler, *J. Phys. D: Appl. Phys.*, 2010, **43**, 264001.
4 A. Stupakiewicz, K. Szerenos, D. Afanasiev, A. Kirilyuk and A. V. Kimel, *Nature*, 2017, **542**, 71.
5 O. Kamada, T. Nakaya and S. Higuchi, *Sens. Actuators, A*, 2005, **119**, 345–348.
6 X. L. Zhang, Y. B. Tang, F. Zhang and C. S. Lee, *Adv. Energy Mater.*, 2016, **6**, 1502588.
7 S. E. Shirsath, C. Cazorla, T. Lu and D. Y. Wang, *Nano Lett.*, 2020, **20**, 1262–1271.
8 S. E. Shirsath, J. Zhang, N. Kumar and W. Walukiewicz, *ACS Nano*, 2022, **16**, 15413–15424.
9 I. Muhammad, A. Ali, L. G. Zhou, W. Zhang, P. Kwan and J. Wong, *J. Alloys Compd.*, 2022, **909**, 164797.
10 J. Zhang, X. C. Wang, L. Zhou, G. X. Liu and W. Wu, *Adv. Mater.*, 2022, **34**, 2106728.
11 X. Liu, W. L. Lim, Z. Ge, S. Shen, M. Dobrowolska, J. K. Furdyna, T. Wojtowicz, K. M. Yu and W. Walukiewicz, *Appl. Phys. Lett.*, 2005, **86**, 112512.
12 C. H. Du, R. Adur, H. L. Wang, A. J. Hauser, F. Y. Yang and P. C. Hammel, *Phys. Rev. Lett.*, 2013, **110**, 147204.
13 H. L. Wang, C. H. Du, P. C. Hamme and F. Y. Yang, *Phys. Rev. B: Condens. Matter Mater. Phys.*, 2014, **89**, 134404.
14 G. F. Dionne, *IEEE Trans. Magn.*, 2011, **47**, 272–278.
15 E. Popova, N. Keller, F. Gendron, L. Thomas, M. C. Brianso, M. Guyot, M. Tessier and S. S. P. Parkin, *J. Vac. Sci. Technol.*, 2001, **19**, 2567–2570.

16 A. Kehlberger, K. Richter, M. C. Onbasli, G. Jakob, D. H. Kim and T. Goto, *et al.*, *Phys. Rev. Appl.*, 2015, **4**, 014008.
17 K. Maeto, A. Itoh, S. Koike and F. Inoue, *IEEE Trans. Magn.*, 1987, **2**, 784–790.
18 M. Kubota, A. Tsukazaki, F. Kagawa, K. Shibuyay, Y. Tokunaga, M. Kawasaki and Y. Tokura, *Appl. Phys. Express*, 2012, **5**, 103002.
19 G. F. Dionne, *J. Appl. Phys.*, 1979, **50**, 4263–4272.
20 E. R. Callen, W. Coleman, A. E. Clarkand, B. Desavage and H. B. Callen, *Phys. Rev.*, 1963, **130**, 1735.
21 C. T. Wang, X. F. Liang, Y. Zhang, X. Liang and Y. P. Zhu, *et al.*, *Phys. Rev. B*, 2017, **96**, 224403.
22 R. B. Borade, S. B. Kadam, D. S. Wagare, R. H. Kadam and S. E. Shirsath, *et al.*, *J. Mater. Sci.: Mater. Electron.*, 2019, **30**, 19782–19791.
23 R. B. Borade, S. E. Shirsath, G. Vats, A. S. Gaikwad and S. M. Patange, *et al.*, *Nanoscale Adv.*, 2019, **1**, 403–413.
24 M. Copel, M. C. Reuter, E. Kaxiras and R. M. Tromp, *Phys. Rev. Lett.*, 1989, **63**, 632–635.
25 H. Nelson, *RCA Rev.*, 1963, **24**, 603–615.
26 J. Vilms and J. Garrett, *Solid-State Electron.*, 1972, **15**, 443–455.
27 S. Blank and J. Nielsen, *J. Cryst. Growth*, 1972, **17**, 302–311.
28 W. R. Holmquist, C. F. Kooi and R. W. Moss, *J. Am. Ceram. Soc.*, 1961, **44**, 194–196.
29 M. H. Fang, J. T. Huang, Z. H. Huang, Y. G. Liu, B. Jiang and P. Peng, *Key Eng. Mater.*, 2008, **368**, 588–590.
30 R. Nazlan, M. Hashim, N. H. Abdullah, I. R. Ibrahim and I. Ismail, *Adv. Mater. Res.*, 2012, **501**, 324–328.
31 W. Ali, M. Othman, M. F. Ain, N. S. Abdullah and Z. A. Ahmad, *J. Am. Ceram. Soc.*, 2016, **99**, 315–323.
32 R. Hergt, *Cryst. Res. Technol.*, 1980, **15**, 673–682.
33 P. Goernert and F. W. Voigt, *High temperature solution growth of garnets: theoretical models and experimental results*, 1984.
34 I. I. Syvorotka, I. M. Syvorotka and S. B. Ubizskii, *Solid State Phenom.*, 2013, **200**, 250–255.
35 Z. H. Zhang, X. N. Yang, K. H. Liu and R. M. Wang, *Adv. Sci.*, 2022, **9**, 2105201.
36 T. Aichele, A. Lorenz, R. Hergt and P. Gornert, *Cryst. Res. Technol.*, 2003, **38**, 575–587.
37 S. E. Shirsath, X. X. Liu, Y. Yasukawa and S. Li, *et al.*, *Sci. Rep.*, 2016, **6**, 30074.
38 S. E. Shirsath, D. Y. Wang, J. Zhang and A. Morisako, *et al.*, *ACS Appl. Electron. Mater.*, 2020, **11**, 3650–3657.
39 M. Mermoux, A. Crisci, F. Baillet and V. Destefanis, *et al.*, *J. Appl. Phys.*, 2010, **107**, 013512.
40 M. Kubota, K. Shibuya and Y. Tokunaga, *et al.*, *J. Magn. Magn. Mater.*, 2013, **339**, 63–70.
41 Z. Shun, H. Xiyun, Z. Xia, Q. Pingsun, L. Liang and S. Dazhi, *J. Inorg. Mater.*, 2022, **37**, 773–779.
42 G. A. Allen and G. F. Dionne, *J. Appl. Phys.*, 1993, **73**, 6130–6132.
43 A. Ikesue and Y. L. Aung, *J. Am. Ceram. Soc.*, 2018, **101**, 5120–5126.
44 A. Chakravarty, *PhD*, Michigan Technological University, 2015.